Energy Advances

ROYAL SOCIETY OF CHEMISTRY

COMMUNICATION

View Article Online
View Journal | View Issue

Cite this: *Energy Adv.*, 2022, 1, 606

Received 4th July 2022,
Accepted 22nd July 2022

DOI: 10.1039/d2ya00171c

rsc.li/energy-advances

Enhanced lifetime of the zinc–iodine batteries using hydrocarbon cation-exchange polymer-protected zinc anodes†

Qiliang Wei, [ab] Eric Schibli,[c] Binyu Chen [a] and Steven Holdcroft *[a]

The zinc–iodine battery is a cost-effective, safe and scalable energy-storage device, which is nevertheless hindered by dendrite formation on the Zn anode and crossover of triiodide anions to the anode. We report that deposition of a fluorine-free cation-exchange polymer, sulfophenylated poly(phenylene)biphenyl (sPPB), onto the Zn anode serves as a protection layer that significantly suppresses Zn dendrite growth and restricts unwanted reaction of triiodide ions at the anode. sPPB-protected Zn anodes possess a relatively low charging polarization overpotential, which is attributed to a lower energy barrier for the desolvation of Zn ions, as supported by DFT calculations. sPPB-protected Zn anodes exhibit a >10× lifetime compared to bare Zn anodes in the Zn//Zn symmetric cells. Aqueous sPPB-protected zinc–iodine batteries deliver an initial capacity of 174 mA h g^{-1} at 5C and retain 131 mA h g^{-1} after 4000 cycles.

Introduction

Lithium-ion batteries (LIBs) are a dominant energy carrier of choice for many applications, ranging from portable electronics and smart grid energy storage to electric vehicles.[1–3] However, the employment of flammable organic electrolytes in LIBs imposes safety issues.[4] Moreover, the cost of LIBs is relatively high due to the cost of lithium resources and transition metals. The development of low-cost, safe, aqueous electrolyte-based metal-ion batteries is experiencing a renewed interest because of these challenges.[5–8] In this regard, aqueous Zn anode-based devices, with their inherent safety, high theoretical capacity (820 mA h g_{Zn}^{-1}) and useful redox potential of Zn (−0.76 V *vs.* SHE) hold promise for development of clean energy storage devices.[9–12] On the complementary cathode side, significant research has been performed on manganese oxides,[13–15] vanadium oxides,[16,17] Prussian blue,[18–20] quinone derivatives,[21,22] and polyanion compounds,[23,24] reporting great progress in each type. Zn-Anode based flow batteries are another class of Zn energy storage device,[25–28] where redox electrochemistry is achieved under circulating solutions. Among these, the Zn–I_2 flow battery is attracting attention due to the fast reversible kinetics of the I^-/I_3^- redox couple, its high theoretical capacity (211 mA h g^{-1}) and potential (0.54 V).[25,29–33] Moreover, iodine is an abundant element, with sea water holding ∼55 μg per liter.[34]

On the downside, the iodide or polyiodide (triiodide) species formed during charge/discharge processes dissolve into electrolytes and diffuse to the anode side, resulting in unwanted side reactions, self-discharge and capacity decay of the battery, not dissimilar to the deleterious 'shuttling' process of polysulfide ion species in Li–S batteries.[35,36] To address these issues, porous carbon materials have been used at the cathode to confine iodide ions and localize the reversible reaction of I^- to I_2.[37–39] Nonetheless, due to the weak interaction between iodine and the host materials, this strategy alone cannot satisfactorily suppress the shuttling and reaction of iodide species to/at the anode, which is exacerbated by Zn dendrite growth at the anode. In an attempt to resolve both these issues, dendrite formation and reaction of iodide species at the anode, Yang *et al.*[34] recently investigated a metal–organic framework (MOF)-based multifunctional membrane possessing ultrasmall pore size to restrict access of iodide ion species at the Zn anode. Despite an observable improvement in the lifetime of the Zn–I_2 cells and proof of principle, the MOFs used are prohibitively expensive to be employed at scale.

An alternate triiodide ion blocking material is a negatively-charged cation exchange polymer. Perfluorosulfonic acid (PFSA)-based Nafion, is a well-studied cation exchange polymer of this kind. Cui and co-workers[40] have employed Nafion to protect the Zn anode, however, due to its internal 4 nm ion channels, it does not guarantee good electrochemical performance, and there are growing environmental concerns associated with the use of

[a] *Department of Chemistry, Simon Fraser University, Burnaby, BC, V5A 1S6, Canada. E-mail: holdcrof@sfu.ca*
[b] *Institute of Micro/Nano Materials and Devices, Ningbo University of Technology, Ningbo, 315211, Zhejiang, China*
[c] *Department of Physics, Simon Fraser University, Burnaby, BC, V5A 1S6, Canada*

† Electronic supplementary information (ESI) available. See DOI: https://doi.org/10.1039/d2ya00171c

fluorinated compounds. A chemically-stable, fluorine-free cation exchange membrane is sought to improve the performance of aqueous Zn batteries by way of an anode protective layer to suppresses dendrite growth and suppress deleterious reactions of anions at the anode.

Our research group has been actively engaged in the design and synthesis of hydrocarbon membranes with high chemical stability for nearly three decades, and has recently focused on ion-containing polyphenylenes using pre-sulfonated monomers to yield structurally-defined cation exchange polymers which possess high degrees of sulfonation without dissolution.[41] The strategy enables incorporation of a wide range property-modifying groups into the main chain. These allow for modifying the length and bulkiness of the phenylene spacer that separates the acid-baring units along the chain,[42,43] branching,[44] and for controlling the rigidity of the main chain.[44] Herein, we investigate a fluorine-free hydrocarbon ionomer, sulfophenylated poly(phenylene)biphenyl (sPPB),[42] as a protective layer on the Zn anode, and study its effect in both Zn//Zn symmetric cells and Zn//I_2 cell devices. The sPPB layer is proposed to simultaneously suppress reaction of I_3^- species at the anode (Fig. 1) and enhance the uniform plating/stripping of the Zn anode so as to limit dendrite formation.

Results and discussion

In this work, sulfophenylated poly(phenylene)biphenyl (sPPB) is deposited on the Zn surface to form Zn-sPPB as illustrated in Fig. 1a and described in the Experimental section (ESI†). The protection mechanism of sPPB to repel the triiodide (I_3^-) crossover for Zn//I_2 battery is based on the Donnan effect, as illustrated in Fig. 1b. The morphology of bare Zn and Zn-sPPB was characterized by SEM. After coating, the rough and uneven surface of bare Zn (Fig. 1c) was rendered relatively uniform by the sPPB film (Fig. 1d). Upon closer inspection, (see Fig. S1, ESI†) sPPB exists in globular form with particle sizes in the nm range. With the assistance of a focused ion beam (FIB), the cross-section view of the Zn-sPPB can be observed (Fig. 1e), and a thickness of the sPPB is ~2.7 μm determined. The low content of Zn (~1 at%) by EDX indicates the successful coating of sPPB (Table S1, ESI†). XRD diffractograms of both bare Zn and Zn-sPPB (Fig. S3, ESI†) reveals only characteristic peaks of Zn. Attenuated total reflection (ATR) spectra of sPPB and Zn-sPPB (Fig. S4, ESI†) reveal multiple absorption peaks for sPPB between ~1000–1030 cm^{-1}, assigned to R–SO_3^-.

Electrochemical cells with bare Zn and Zn-sPPB were assembled in symmetric coin cells with 1 M $ZnSO_4$ as

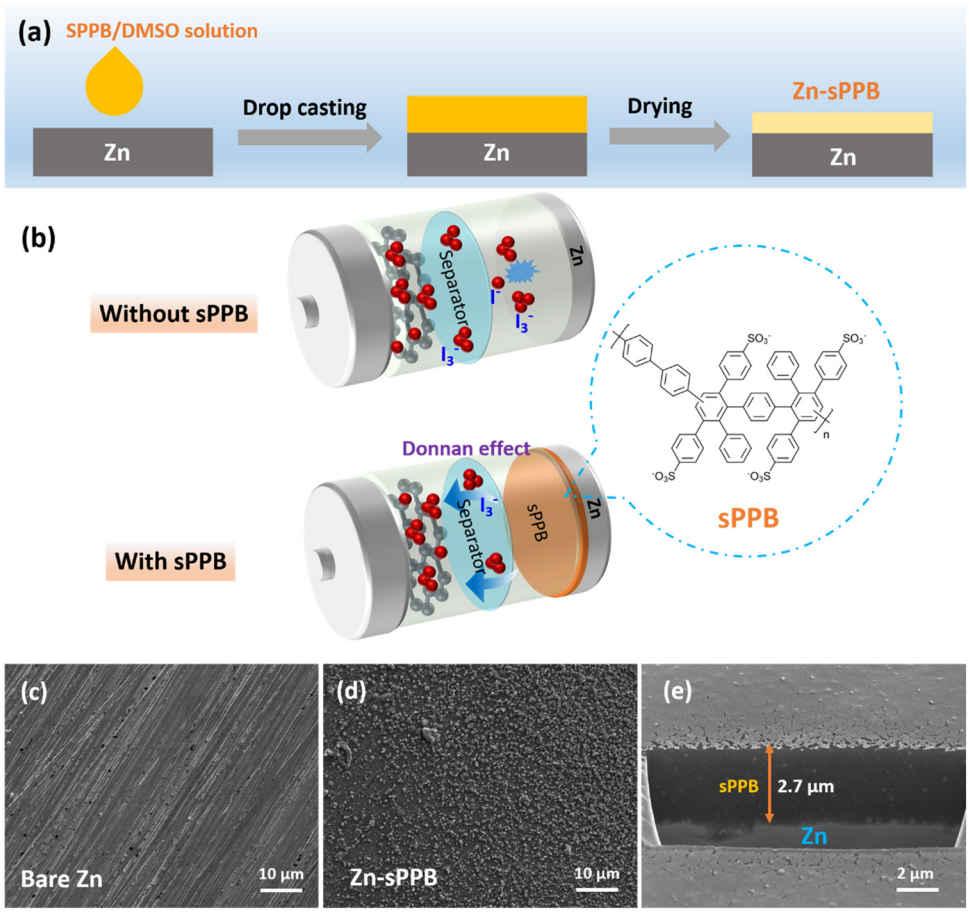

Fig. 1 (a) Scheme of the sPPB coating process on Zn metal; (b) mechanism of Zn–I_2 batteries with bare Zn and sPPB protected Zn as anodes. SEM images of (c) the bare Zn, (d) top-view of sPPB protected Zn, and (e) cross-section-view of sPPB coated Zn.

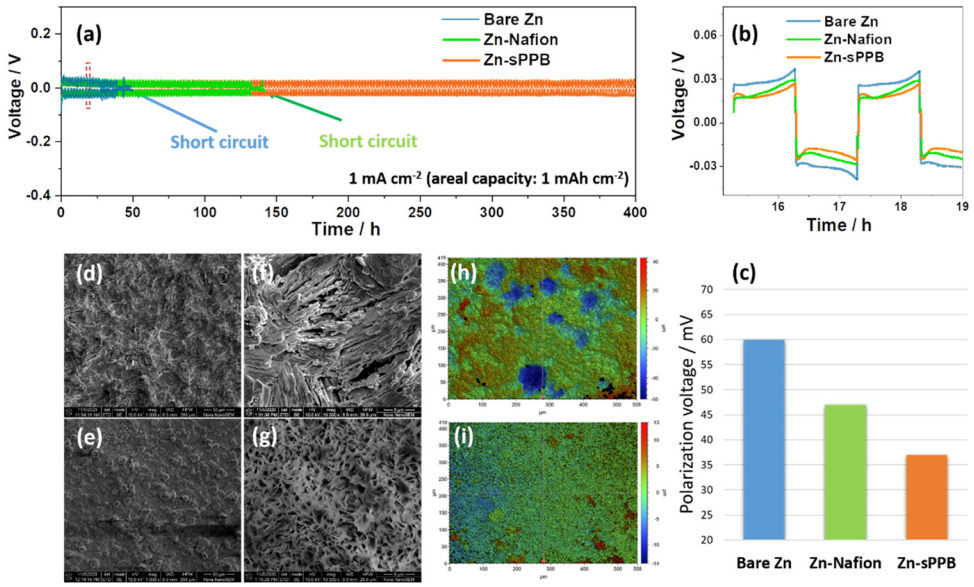

Fig. 2 (a) The cycling performance of bare Zn, Zn-Nafion, Zn-sPPB at 1 mA cm^{-2} with areal capacity of 1 mA h cm^{-2}; (b and c) the comparison of Zn plating/stripping profiles and the polarization voltage values for bare Zn, Zn-Nafion, and Zn-sPPB electrodes between 15–19 h. (d–i) SEM, and height mapping images of (d, f and h) bare Zn after 40 h cycling and (e, g and i) Zn-sPPB after 80 h cycling in the symmetrical cells.

supporting electrolyte, and subjected to repeated plating/stripping at 1 mA cm^{-2}. The corresponding performance curves are presented in Fig. 2a. Cells constructed with Zn-Nafion were also examined for comparison. Failure of the cell due to short-circuiting of the electrodes occurred after 40 h of testing for the cells containing bare Zn electrodes, and after 130 h testing for the Zn-Nafion cells; whereas Zn-sPPB cells were stable for >400 h without any sign of short circuit failure. Even under a higher current density, a similar stability can be achieved (Fig. S5, ESI†). Notably, the polarization voltages values of these symmetric cells are subtly different. From Fig. 2b and c, the polarization voltage of the Zn-sPPB symmetric cell is determined to be 37 mV, which is lower than that of the bare Zn cell (60 mV) and Zn-Nafion cell (47 mV). The smaller polarization indicates a lower energy barrier for electrochemical reduction and oxidation processes associated with Zn plating and Zn dissolution. SEM images of the electrodes were taken on deconstructed cells after 40 h for bare Zn cells and after 80 h for Zn-sPPB. As shown in Fig. 2d and f, bare Zn had formed randomly dendritic or rod-like structures, while Zn-sPPB electrodes possessed a dimpled but uniform structure (Fig. 2e and g). The surface topography was analyzed by the profilometry, (Fig. 2h and i). The surface of the bare Zn exhibited a 95 μm differential from valley to peak; Zn-sPPB electrodes exhibited only a 27 μm differential (after twice the length of the cycling time). Detailed profiles can be found in Fig. S6 and S7 (ESI†). These results demonstrate that dendrite growth causes short circuiting of the bare Zn-based cell, and that the sPPB layer reduces dendrite growth. Insight into the protective function of the sPPB layer on Zn deposition behavior can also be proved by a different substrate Ti. Here, the Zn nucleation process was studied in a three-electrode system with bare Ti (or Ti-sPPB coated Ti) serving as the working electrode, Zn as the counter electrode, and SCE as the reference electrode. 1 M $ZnSO_4$ was used as the electrolyte. As shown in the cyclic voltammetry (CV) in Fig. S8 (ESI†), the crossing point P is the crossover potential where the current is zero, and Q (Q') is the point where Zn starts to deposit. The distance between P and Q (or Q') (termed as nucleation overpotential[45]) can be used to gain insights into the polarization behavior of the electrode.[46,47] The nucleation overpotential of the sPPB coated Ti is 24 mV lower than that of the bare Ti, indicating the depolarizing effect of sPPB. Chronoamperometry (CA) was conducted to study the Zn deposition growth mechanism (Fig. S9, ESI†). The rapidly-increasing current density for the bare Ti suggests a faster dendrite growth process after 100 s. While for the sPPB coated Ti electrode, after $\sim$55 s, a stable current density of $\sim$18 mA cm^{-2} was observed, indicating a uniform rate of Zn deposition. The influence of the sPPB is to coordinate the deposition of Zn^{2+} uniformly under a reduced rate leading to an increased number of nucleation sites and formation of a uniform Zn layer.

In order to investigate rejection of anionic triiodide species by films of sPPB, a H-type cell was assembled as shown in Fig. S10 (ESI†). The left chamber was filled with the 1 M KI + 0.1 M I_2 (dark brown); and the right, with K_2SO_4 electrolyte (colorless). In one cell, the chambers were separated by a separator comprised of glass fiber (GF), and in the other cell the separator was replaced by a composite of glass fiber and sPPB. For the cells separated by glass fiber, the color of the solution in the right chamber turns light brown after several minutes, becoming dark brown after 1 h. In contrast, the cell with the glass fiber/sPPB composite membranes exhibits much reduced crossover of triiodide ions even after 4 h. Quantitate analysis of the crossover of triiodide species from the H-cell was calculated using the starch titration method (described in the ESI†), and the result is shown in Fig. 3a. Employing a glass fiber

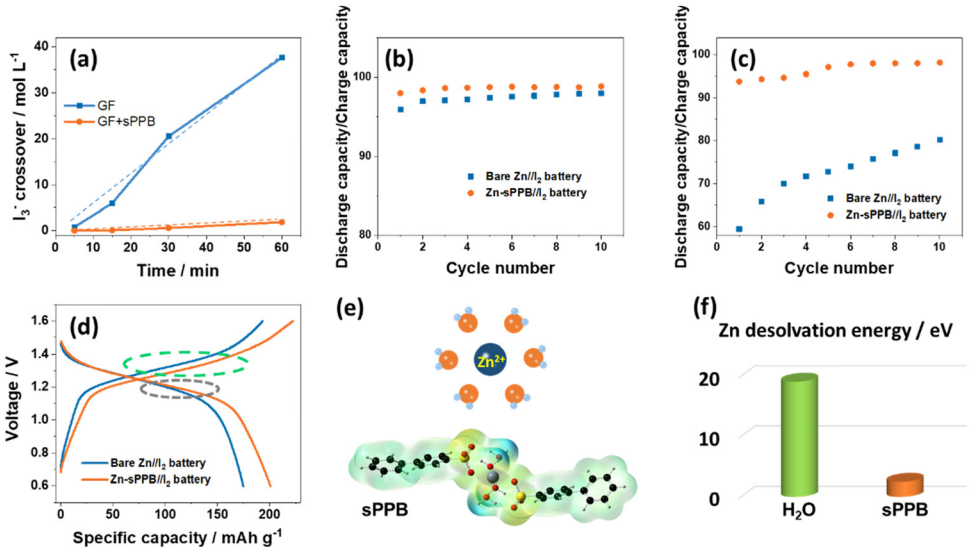

Fig. 3 (a) Crossover of triiodide anions crossover through a glass fibre (GF) and glass fibre/sPPB composite) (GF + sPPB) separator with time. (b) Coulombic efficiency of the Zn//I_2 battery with 2 h holding after each full charge state. (c) Coulombic efficiency of the Zn//I_2 battery with 8 h holding after each full charge state. (d) Galvanostatic discharge–charge profiles of the bare Zn//I_2 battery and Zn-sPPB//I_2 battery obtained in the 2nd cycle at 1C. (e) Schematic illustration of the coordination environment in water and DFT-optimized geometry with sPPB. (f) Desolvation energy of Zn^{2+} in water and sPPB.

separator, the triiodide crossover rate is 37.8 mol L^{-1} min^{-1}; with the glass fiber/sPPB composite separator, the rate of triiodide crossover is decreased to 1.8 mol L^{-1} min^{-1}.

Zn–I_2 coin-cells were assembled using Zn as anode, I_2/KI within active carbon as cathode, and $ZnSO_4$ as electrolyte. Charge–discharge cycling was first conducted at 1C (211 mA g^{-1}), holding for 2 h or 8 h after each full charge state. The test protocol is illustrated in Fig. S11 (Protocol A) and S12 (Protocol B) (ESI†). The ratio of discharge capacity to charge capacity is presented in Fig. 3b and c. For Protocol A, with a shorter holding time, Zn-sPPB//I_2 cell has a little higher ratio (~99%) in the whole process than that of bare Zn//I_2 cell (95–97%); in Protocol B with a longer holding time (8 h) after each full charge, the discharge capacity/charge capacity between Zn-sPPB//I_2 cell and bare Zn//I_2 cell is increased (~96% *vs.* <80%), indicating suppression of mobile of I_3^- species by the sPPB layer on the Zn anode. This is consistent with the visualized I_3^- crossover experiment in the H-type cell shown in Fig. S10 (ESI†) and Fig. 3a, in which the penetration of I_3^- is significantly hindered by sPPB. The galvanostatic discharge–charge profiles of the bare Zn//I_2 cell and Zn-sPPB//I_2 cell are displayed in Fig. 3d. By comparison, it can be observed that the discharge profiles of these two cells are almost in the same position (meaning they exhibit a similar discharge plateau, the grey circle), and the lower charging–discharging polarization gap of the Zn-sPPB//I_2 cell originates from the charging process (green circle). Upon charging, the reaction on the anode corresponds to the reduction process Zn^{2+} to Zn, during which desolvation of Zn^{2+} is important.[40] Thus, the energy to desolvate Zn^{2+} was calculated by density functional theory (DFT) as described in the ESI.† In $ZnSO_4$ electrolyte, six water molecules surround the Zn^{2+} ion, leading to a high desolvation energy (19.1 eV, Fig. 3f). In the presence of sPPB layer, two $-SO_3^-$ groups and four water molecules coordinate the Zn^{2+}, leading to a decreased desolvation energy of 2.5 eV. Nafion also possesses a $-SO_3^-$ head group, so we further compared the desolvation energies of Nafion and sPPB, the result of which is shown in Fig. S13 (ESI†), wherein a lower desolvation energy of Zn^{2+} in the presence of sPPB is observed.

Fig. 4a shows cyclic voltammograms of typical Zn-sPPB//I_2 coin-cell recorded at different scan rates (0.2, 0.3, 0.5, 1.0, 2.0, 3.0 mV s^{-1}). Anodic and cathodic peaks are observed at ~1.2 V and ~1.3 V, respectively. The peak current increases with increasing scan rate, following a power law relationship: $i = av^b$.[48] The b value typically falls between 0.5 and 1.0; with values of 0.5 representing a diffusion-controlled process as is observed for species dissolved in a medium; as opposed to values of 1.0, which are observed for surface bound-species or a capacitive dominant charge storage process. After a formula conversion, it can be expressed as:

$$\log i = \log a + b \log v \quad (1)$$

b values were determined from the slope of the plot of $\log i$ *versus* $\log v$, illustrated in Fig. 4b and found to be 0.837 and 0.820 (both are close to 1) for the anodic and cathodic redox processes, respectively. b value close to 1 indicate a high occurrence of the redox reactions on the surface or near-surface region of electrodes, in which case the faradaic process of the electrode in electrolyte is faster than a bulk phase transformation or ion-diffusion through the solid upon charging/discharging.[49,50] This implies that the charge stored in the redox process of the Zn–I_2 battery is simultaneously controlled by capacitive and diffusion contributions, but governed by the surface-induced capacitive behavior. The current i is therefore

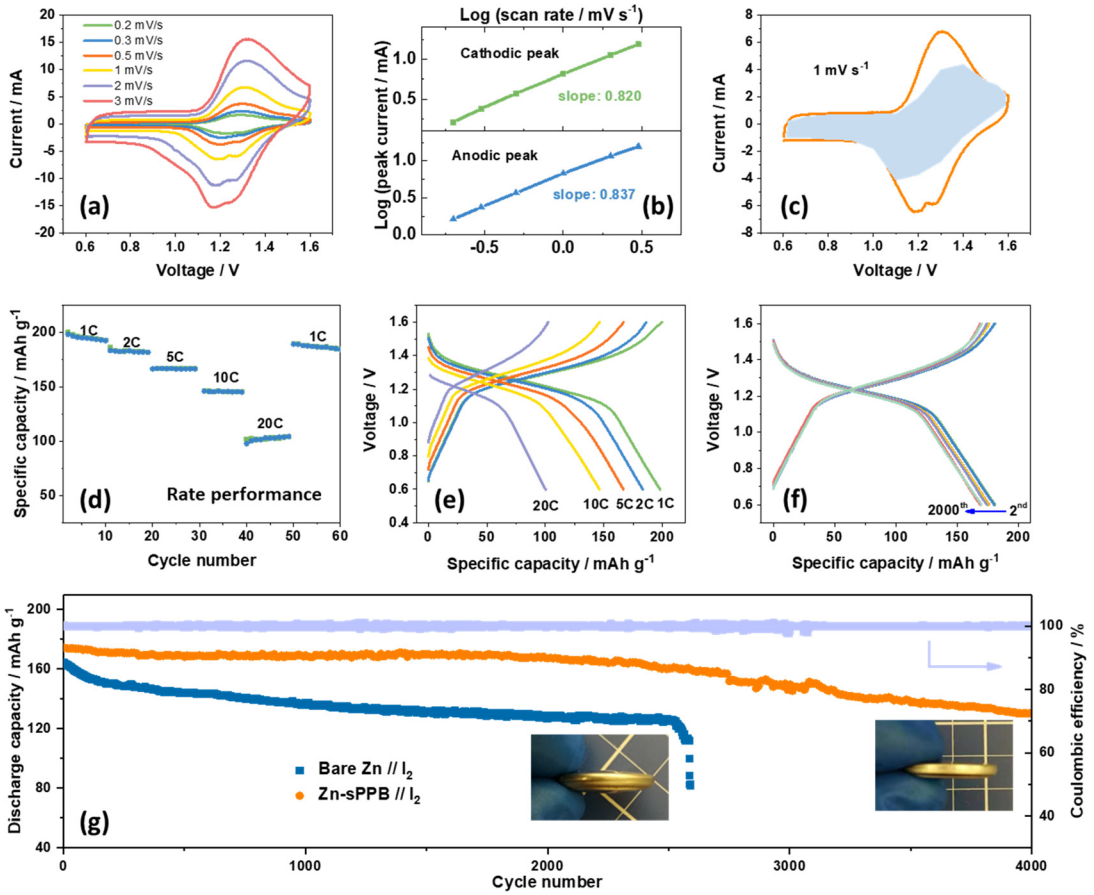

Fig. 4 (a) CV curves of Zn-sPPB//I_2 batteries at different scan rates. (b) log i and log v plots at anodic/cathodic peak currents. (c) CV curve with the pseudocapacitive (blue-shaded) contribution at 1 mV s^{-1}. (d) Rate performance of the Zn-sPPB//I_2 battery. (e) Galvanostatic discharge–charge profiles of the Zn-sPPB//I_2 battery at different current densities. (f) Galvanostatic discharge–charge profiles of the Zn-sPPB//I_2 obtained in the first 2000 cycles at 5C. (g) Comparison of long-term cycling performance at 5C (1055 mA g^{-1}) with bare Zn and Zn-sPPB anodes (coulombic efficiency corresponds to the Zn-sPPB//I_2 cell).

regarded as the combination of a capacitive contribution (k_1) and a diffusion contribution (k_2):

$$i = k_1 v + k_2 v^{1/2} \quad (2)$$

In this way, the ratio of the capacitive contribution to the total charge stored in each voltage at a given scan rate can be determined. The capacitive current profile *versus* voltage of the Zn-sPPB//I_2 battery is shown in Fig. 4c, and the calculated capacitive contribution at 1 mV s^{-1} is calculated as high as 71.6%. This capacitive-dominant process is caused by the surface-induced reaction of the I^-/I_3^- redox occurring in the abundant pores of the activated carbon host, which provide a high specific surface area and well favorable morphology that allows electrolyte access into the inner surface of the electrode.[51] In Fig. 4d, the specific capacities of achieved at 1C, 2C, 5C, 10C and 20C are plotted to be 195, 182, 167, 145 and 102 mA h g^{-1}, respectively, and when the current density is reverted to 1C, a high capacity of 190 mA h g^{-1} is observed. The corresponding charge/discharge voltage profiles are shown in Fig. 4e. A long cycle lifetime measurement was carried out at 5C and the performances shown in Fig. 4f and g. As illustrated in Fig. 4f, the specific capacity for the first 2000 cycles remains similar to its initial value, and the voltage plateaus overlap indicating negligible degradation. After 4000 cycles, the specific capacity of the Zn-sPPB//I_2 battery is maintained at 131 mA h g^{-1}, and the coulombic efficiency is unchanged at ~100% over the entire cycle life. These data indicate the Zn-sPPB//I_2 battery cell profits from the repulsion of I_3^- by sPPB, to provide a stable performance. In the absence of the sPPB film, the specific capacity of the bare Zn//I_2 battery decreases much more rapidly (Fig. S14, ESI†), and the bare Zn//I_2 cell fails after about 2600 cycles, most likely due to a short circuit caused by Zn dendrite growth and side reactions that produce gases, as indicted by the cell which is significantly swollen after 2600 cycles as indicating in the inset of Fig. 4f). In contrast, the Zn-sPPB//I_2 cell operates stably through 4000 cycles with a 75.3% capacity retention and without swelling of the cell.

To further understand the function of sPPB during charge/discharge cycles of the Zn-sPPB//I_2 battery, XPS and ATR measurements were performed on the Zn-sPPB electrode during different charge/discharge states as marked in Fig. S15 (ESI†). XPS high-resolution spectra reveals the binding energy

of the S 2s (Fig. S15b, ESI†) (S from the pendant SO_3^- group of sPPB) shifts to a higher energy (from 232.3 eV to 233.4 eV) during the charging (Zn^{2+}/Zn reduction process) commensurate with increasing applied voltage, while the Zn 2p peaks simultaneously shifts to a lower binding energy (Fig. S15c, ESI†). Notably, the appearance of two split peaks in the Zn 2p spectra during charging is reasonably assigned to the coordination structure of the $-SO_3^-$–Zn^{2+}–SO_3^-, which we interpret to indicate that the sulfonate groups on sPPB serve as a solvent sheath for Zn^{2+}. In the following discharge process, the signals revert to their original binding energy, demonstrating a highly reversible process. The negligible shift of wavenumber in the range of $\sim$1000–1030 cm^{-1} (Fig. S15d, ESI†) indicates the stability of sPPB during charging/discharging.

Conclusion

In summary, electrochemical measurements, spectroscopic and imaging analyses, and DFT simulations support the hypothesis that sPPB facilitates the desolvation of Zn^{2+}, playing a vital role in improving the Zn plating process by suppressing the dendrite growth, and serves to repel triiodide species against reaching the Zn anode – all of which enhance the cycle life of the Zn//I_2 battery while maintaining the high specific capacity.

Conflicts of interest

There are no conflicts to declare.

Acknowledgements

This work was supported by the Natural Sciences and Engineering Research Council of Canada (NSERC) (Grant RGPIN-2018-03698) and made use of facilities in 4D LABS, SFU. The authors thank Dr Simon Cassegrain for the ATR measurements and fruitful discussions; and Dr Michael Adamski for synthesizing sPPB polymer.

References

1 A. Manthiram, *Nat. Commun.*, 2020, **11**, 1–9.
2 B. Wu, X. Yang, X. Jiang, Y. Zhang, H. Shu, P. Gao, L. Liu and X. Wang, *Adv. Funct. Mater.*, 2018, **28**, 1803392.
3 Y. Fu, Q. Wei, G. Zhang and S. Sun, *Adv. Energy Mater.*, 2018, **8**, 1703058.
4 P. Lyu, X. Liu, J. Qu, J. Zhao, Y. Huo, Z. Qu and Z. Rao, *Energy Storage Mater.*, 2020, **31**, 195–220.
5 C. Liu, X. Wang, W. Deng, C. Li, J. Chen, M. Xue, R. Li and F. Pan, *Angew. Chem., Int. Ed.*, 2018, **130**, 7164–7168.
6 C. Yan, C. Lv, L. Wang, W. Cui, L. Zhang, K. N. Dinh, H. Tan, C. Wu, T. Wu and Y. Ren, *J. Am. Chem. Soc.*, 2020, **142**, 15295–15304.
7 J. Huang, Z. Wang, M. Hou, X. Dong, Y. Liu, Y. Wang and Y. Xia, *Nat. Commun.*, 2018, **9**, 1–8.
8 Y. Li, Z. Wang, Y. Cai, M. E. Pam, Y. Yang, D. Zhang, Y. Wang and S. Huang, *Energy Environ. Mater.*, 2022, **0**, 1–29.
9 Z. Wang, J. Huang, Z. Guo, X. Dong, Y. Liu, Y. Wang and Y. Xia, *Joule*, 2019, **3**, 1289–1300.
10 J. Hao, X. Li, S. Zhang, F. Yang, X. Zeng, S. Zhang, G. Bo, C. Wang and Z. Guo, *Adv. Funct. Mater.*, 2020, 2001263.
11 Y. Yin, S. Wang, Q. Zhang, Y. Song, N. Chang, Y. Pan, H. Zhang and X. Li, *Adv. Mater.*, 2020, **32**, 1906803.
12 J. Ming, J. Guo, C. Xia, W. Wang and H. N. Alshareef, *Mater. Sci. Eng., R*, 2019, **135**, 58–84.
13 T. Xiong, Y. Zhang, W. S. V. Lee and J. Xue, *Adv. Energy Mater.*, 2020, **10**, 2001769.
14 G. Liu, H. Huang, R. Bi, X. Xiao, T. Ma and L. Zhang, *J. Mater. Chem. A*, 2019, **7**, 20806–20812.
15 Y. Fu, Q. Wei, G. Zhang, X. Wang, J. Zhang, Y. Hu, D. Wang, L. Zuin, T. Zhou and Y. Wu, *Adv. Energy Mater.*, 2018, **8**, 1801445.
16 F. Wan and Z. Niu, *Angew. Chem., Int. Ed.*, 2019, **58**, 16358–16367.
17 L. Wang, K.-W. Huang, J. Chen and J. Zheng, *Sci. Adv.*, 2019, **5**, eaax4279.
18 Z. Liu, P. Bertram and F. Endres, *J. Solid State Electrochem.*, 2017, **21**, 2021–2027.
19 L.-P. Wang, P.-F. Wang, T.-S. Wang, Y.-X. Yin, Y.-G. Guo and C.-R. Wang, *J. Power Sources*, 2017, **355**, 18–22.
20 G. Zampardi and F. La Mantia, *Curr. Opin. Electrochem.*, 2020, **21**, 84–92.
21 Q. Zhao, W. Huang, Z. Luo, L. Liu, Y. Lu, Y. Li, L. Li, J. Hu, H. Ma and J. Chen, *Sci. Adv.*, 2018, **4**, eaao1761.
22 C. Han, H. Li, R. Shi, T. Zhang, J. Tong, J. Li and B. Li, *J. Mater. Chem. A*, 2019, **7**, 23378–23415.
23 H. Y. Shi, Y. Song, Z. Qin, C. Li, D. Guo, X. X. Liu and X. Sun, *Angew. Chem., Int. Ed.*, 2019, **58**, 16057–16061.
24 G. Li, Z. Yang, Y. Jiang, C. Jin, W. Huang, X. Ding and Y. Huang, *Nano Energy*, 2016, **25**, 211–217.
25 B. Li, Z. Nie, M. Vijayakumar, G. Li, J. Liu, V. Sprenkle and W. Wang, *Nat. Commun.*, 2015, **6**, 6303.
26 K. Gong, X. Ma, K. M. Conforti, K. J. Kuttler, J. B. Grunewald, K. L. Yeager, M. Z. Bazant, S. Gu and Y. Yan, *Energy Environ. Sci.*, 2015, **8**, 2941–2945.
27 Z. Yuan, Y. Yin, C. Xie, H. Zhang, Y. Yao and X. Li, *Adv. Mater.*, 2019, **31**, 1902025.
28 Y. Cheng, N. Zhang, Q. Wang, Y. Guo, S. Tao, Z. Liao, P. Jiang and Z. Xiang, *Nano Energy*, 2019, **63**, 103822.
29 M. Xing, Z. Zhao, Y. Zhang, J. Zhao, G. Cui and J. Dai, *Mater. Today Energy*, 2020, 100534.
30 G.-M. Weng, Z. Li, G. Cong, Y. Zhou and Y.-C. Lu, *Energy Environ. Sci.*, 2017, **10**, 735–741.
31 C. Xie, Y. Liu, W. Lu, H. Zhang and X. Li, *Energy Environ. Sci.*, 2019, **12**, 1834–1839.
32 C. Xie, H. Zhang, W. Xu, W. Wang and X. Li, *Angew. Chem., Int. Ed.*, 2018, **130**, 11341–11346.
33 J. Zhang, G. Jiang, P. Xu, A. G. Kashkooli, M. Mousavi, A. Yu and Z. Chen, *Energy Environ. Sci.*, 2018, **11**, 2010–2015.
34 H. Yang, Y. Qiao, Z. Chang, H. Deng, P. He and H. Zhou, *Adv. Mater.*, 2020, **32**, 2004240.
35 N. Kang, Y. Lin, L. Yang, D. Lu, J. Xiao, Y. Qi and M. Cai, *Nat. Commun.*, 2019, **10**, 1–10.
36 C. V. Pham, L. Liu, B. Britton, M. Walter, S. Holdcroft and S. Thiele, *Sustainable Energy Fuels*, 2020, **4**, 1180–1190.

37 C. Bai, F. Cai, L. Wang, S. Guo, X. Liu and Z. Yuan, *Nano Res.*, 2018, **11**, 3548–3554.
38 H. Pan, B. Li, D. Mei, Z. Nie, Y. Shao, G. Li, X. S. Li, K. S. Han, K. T. Mueller and V. Sprenkle, *ACS Energy Lett.*, 2017, **2**, 2674–2680.
39 Y. Li, L. Liu, H. Li, F. Cheng and J. Chen, *Chem. Commun.*, 2018, **54**, 6792–6795.
40 Y. Cui, Q. Zhao, X. Wu, X. Chen, J. Yang, Y. Wang, R. Qin, S. Ding, Y. Song and J. Wu, *Angew. Chem., Int. Ed.*, 2020, **132**, 16737–16744.
41 T. J. Skalski, B. Britton, T. J. Peckham and S. Holdcroft, *J. Am. Chem. Soc.*, 2015, **137**, 12223–12226.
42 M. Adamski, T. J. G. Skalski, B. Britton, T. J. Peckham, L. Metzler and S. Holdcroft, *Angew. Chem., Int. Ed.*, 2017, **56**, 9058–9061.
43 T. J. G. Skalski, M. Adamski, B. Britton, E. M. Schibli, T. J. Peckham, T. Weissbach, T. Moshisuki, S. Lyonnard, B. J. Frisken and S. Holdcroft, *ChemSusChem*, 2018, **11**, 4033–4043.
44 M. Adamski, T. J. G. Skalski, E. M. Schibli, M. Killer, Y. Wu, N. Peressin, B. J. Frisken and S. Holdcroft, *J. Membr. Sci.*, 2020, **595**, 117539.
45 D. MacKinnon, R. Morrison, J. Mouland and P. Warren, *J. Appl. Electrochem.*, 1990, **20**, 728–736.
46 Z. Zhao, J. Zhao, Z. Hu, J. Li, J. Li, Y. Zhang, C. Wang and G. Cui, *Energy Environ. Sci.*, 2019, **12**, 1938–1949.
47 Z. Cao, X. Zhu, D. Xu, P. Dong, M. O. L. Chee, X. Li, K. Zhu, M. Ye and J. Shen, *Energy Storage Mater.*, 2020, **36**, 132–138.
48 T. Brezesinski, J. Wang, J. Polleux, B. Dunn and S. H. Tolbert, *J. Am. Chem. Soc.*, 2009, **131**, 1802–1809.
49 S. Liu, L. Kang, J. Zhang, E. Jung, S. Lee and S. C. Jun, *Energy Storage Mater.*, 2020, **32**, 167–177.
50 S. Liu, L. Kang, J. Zhang, S. C. Jun and Y. Yamauchi, *ACS Energy Lett.*, 2021, **6**, 4127–4154.
51 J. Gamby, P. L. Taberna, P. Simon, J. F. Fauvarque and M. Chesneau, *J. Power Sources*, 2001, **101**, 109–116.